ACS APPLIED MATERIALS & INTERFACES

Research Article

www.acsami.org

Surface Plasmon Enhanced Organic Solar Cells with a MoO_3 Buffer Layer

Zisheng Su,* Lidan Wang, Yantao Li, Guang Zhang, Haifeng Zhao, Haigui Yang, Yuejia Ma, Bei Chu,* and Wenlian Li

State Key Laboratory of Luminescence and Applications, Changchun Institute of Optics, Fine Mechanics and Physics, Chinese Academy of Sciences, Changchun 130033, P. R. China

Supporting Information

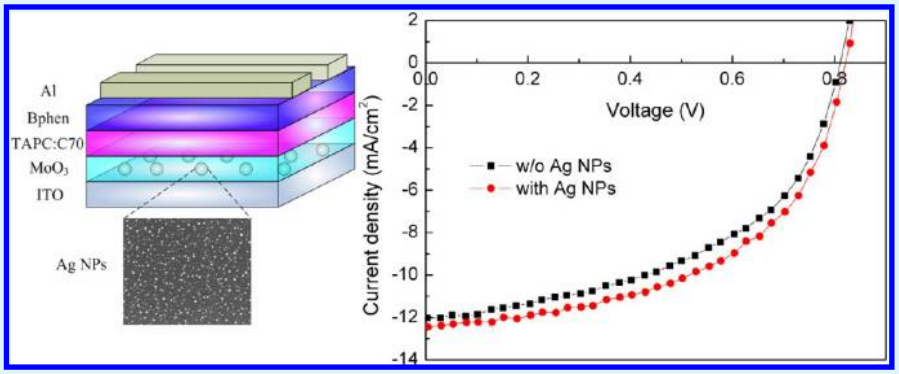

ABSTRACT: High-efficiency surface plasmon enhanced 1,1-bis-(4-bis(4-methyl-phenyl)-amino-phenyl)-cyclohexane:C70 small molecular bulk heterojunction organic solar cells with a MoO_3 anode buffer layer have been demonstrated. The optimized device based on thermal evaporated Ag nanoparticles (NPs) shows a power conversion efficiency of 5.42%, which is 17% higher than the reference device. The improvement is attributed to both the enhanced conductivity and increased absorption due to the near-field enhancement of the localized surface plasmon resonance of Ag NPs.

KEYWORDS: *molybdenum trioxide, organic solar cell, small molecule, localized surface plasmon resonance, metal nanoparticle*

1. INTRODUCTION

Organic solar cells (OSCs) have attracted significant interests because of their potential as a renewable energy source, low-cost and large-scale fabrication, and compatibility with large-area and flexible substrates.[1−5] Over the past two decades, the power conversion efficiency (PCE) of OSCs has steadily improved. A PCE exceeding 10% has been demonstrated by using materials that exhibit broad absorptions with high absorpion coefficients that match the solar spectrum, and by developing new device configurations that provide high exciton dissociation efficiency and charge carriers collection efficiency.[5] The working of OSC involves the formation of excitons after photon absorption, the diffusion of these excitons to the donor/acceptor interface, the dissociation of excitons into electrons and holes, and the collection of electrons and holes at the opposing electrodes. The diffusion and dissociation efficiencies of the photogenerated excitons can approach 100% by using bulk heterojunction structures. Thus the dominant limition of the PCE in an OSC is the absorption efficiency and charge carrier collection efficiency. The charge carrier collection efficiency can be improved by chemical doping of the organic layers[6] or by engineering the metal/organic interface.[7] On the other hand, a simple way to increase the absorption efficiency is to increase the thickness of the organic active layer. This method, however, inevitably increases the charge carrier recombination probability because of the lower charge carrier mobility of organic materials, which limits the fill factor (FF) and the short circuit current density (J_{sc}) and hence the PCE of such cells. Many strategies have been proposed to increase the absorption efficiency of OSCs without increase the thickness of the organic active layer, such as the insertion of an optical spacer to spatially redistribute the light intensity,[8,9] the implementation of periodic nanostructures to increase the optical path length,[10,11] the microcavity effect,[12,13] and photonic crystal geometry.[14,15]

Localized surface plasmons are charge density oscillations confined to metal nanoparticles (NPs) and nanostructures.[16] Localized surface plasmons resonance (LSPR) that is excited by an electric field (light) at an incident wavelength where resonance occurs can result in strong light scattering, in the appearance of intense surface plasmon absorption bands, and in an enhancement of the local electromagnetic fields. The frequency and intensity of LSPR are characteristic of the type of material and are highly sensitive to the size, size distribution,

Received: July 9, 2013
Accepted: December 9, 2013
Published: December 9, 2013

and shape of the nanostructures, as well as the surrounding environments. Surface plasmons triggered by metal NPs have been used to increase the absorption of OSCs.[17−37] The incorporation of metal NPs not only leads to an increased PCE but also improves the stability of the devices.[36,37] Metal NPs can be prepared by chemical and physical methods. Among these, the chemical methods are preferred for the preparation of monodispersed NPs, while physical methods give more polydispersed sizes. OSCs show the greatest enhanced response in the resonance regime of the LSPR.[24−26] This suggests that NPs with a dispersed size distribution may enhance the PCE more owing to the wider range of wavelengths than can trigger the LSPR, where the different sized NPs interact with different wavelengths.[36] Thermal evaporation is a simple and cost-effective physical method for the preparation of metal NPs with dispersed sizes, and has drawn much attention in recent years.[30−34] Such surface plasmon enhanced OSCs generally require a buffer layer to avoid exciton quenching by the metal NPs through electron transfer from the excitons to the metal NPs.[38] Poly(3,4-ethylene dioxythiophene):poly(styrene sulfonate) (PEDOT:PSS) is usually used as such a buffer layer. However, the indium−tin oxide (ITO)/PEDOT:PSS interface is not stable; the acidic PEDOT:PSS can etch ITO, which results in indium contamination of the polymer.[39] MoO_3 is a promising alternative to PEDOT:PSS because it is non-toxic and possesses deep lying electronic states with a suitable work function for contact with various anodes.[40] However, it has rarely been used in surface plamon enhanced OSCs.

Although state-of-the-art polymer solar cells with a PCE exceeding 10% have been demonstrated, it is difficult to achieve even higher efficiency in polymer systems because of the required precise control of the polydispersity index, regioregularity, and molecular weight. These parameters have to be taken into account in thin-film processing, and have a strong correlation to the final photovoltaic performance. Small molecular weight material is an alternative material to polymers.[41−44] Recently, small molecular bulk heterojunction OSCs with a low donor concentration have gained considerable interest, exhibiting PCE as high as 6%.[45−49] However, the PCE needs to be further improved for practical applications. In this research, thermally evaporated Ag NPs with a MoO_3 anode buffer layer is applied to small molecule bulk heterojunction OSCs, and an enhancement in device performance is demonstrated. Such thermal evaporation technology used to prepare the metal NPs and the anode buffer layer is more compatible to the thermal evaporation process of small molecular OSCs, and the whole device can be fabricated in one vacuum system without breaking the vacuum.

2. EXPERIMENTAL DETAILS

Devices were fabricated on patterned ITO-coated glass substrates with a sheet resistance of 15 Ω/sq. The substrates were routinely cleaned followed by UV-ozone treatment for 10 min. The structure of the OSCs used here is ITO/Ag/MoO_3/1,1-bis-(4-bis(4-methyl-phenyl)-amino-phenyl)-cyclohexane (TAPC):C70 (60 nm)/4,7-diphenyl-1,10-phenanthroline (8 nm)/Al (100 nm). The device structure and molecular structures of TAPC and C70 are shown in Figure 1. The weight ratio of TAPC:C70 films was optimized and fixed at 1:19 in this work. A series of devices were fabricated with a nominal thickness of Ag of 0, 0.25, 0.5, 1, and 2 nm, and the thickness of MoO_3 in each device was optimized to achieve the best performance. All the layers, including Ag, were deposited onto the substrates in sequence via thermal evaporation in the vacuum chamber at a pressure of 5×10^{-4} Pa without a vacuum break. Deposition rates and the thickness of the

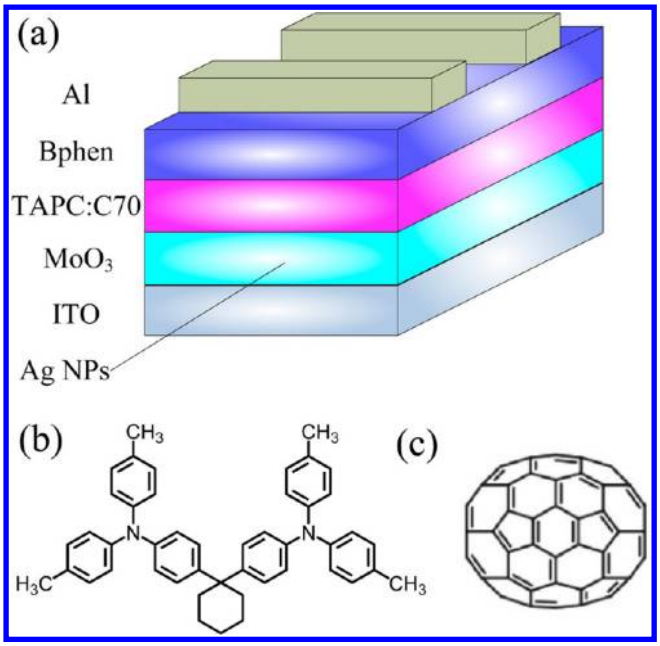

Figure 1. (a) Device structure of the surface plasmon enhanced OSCs, and molecular structures of (b) TAPC and (c) C70.

layers were monitored in situ using oscillating quartz monitors. The evaporation rates were kept at 2−4 Å/s for Ag, 0.2 Å/s for MoO_3, 1 Å/s for the organic layers, and 5 Å/s for the Al cathode. Current-voltage (J−V) characteristics of the devices were measured with a Keithley 2400 source meter both in dark and illuminated with a Xe lamp with an AM 1.5 G filter, and the irradiation intensity was certified to be 100 mW/cm^2. The J−V curves shown here are averages of the data from four devices with the same configuration. The incident photon to current conversion efficiency (IPCE) spectra were performed with a Stanford SR803 lock-in amplifier under monochromatic illumination at a chopping frequency of 130 Hz by a Stanford SR540 chopper. Scanning electron microscopy (SEM) images were measured on a Hitachi S4800. Absorption spectra were recorded with a Shimadzu UV-3101PC spectrophotometer. Steady-state photoluminescent (PL) spectra were measured with a Hitachi F7000 fluorescence spectrophotometer. Transient PL decay was measured with an Edinburgh FL 920 spectrometer at an excitation wavelength of 450 nm by using a hydrogen lamp and the PL emission was detected at 648 nm. The surface topographies were imaged with a Bruker MultiMode 8 atomic force microscope (AFM) in tapping mode. All the measurements were carried out at room temperature under ambient conditions.

3. RESULTS AND DISCUSSION

Figure S1 in the Supporting Information shows the SEM images of Ag films with different thickness on the ITO substrate. All the Ag films present a discontinued island-like morphology. Because of the large grain size of the ITO and high roughness of the ITO surface, it is difficult to distinguish the Ag NPs from the ITO substrate. However, we can still find that the density of the Ag NPs increases with the thickness of Ag film, and the average diameter of the Ag NPs is about 7−8 nm. To demonstrate the morphology of the Ag films, we selected a Si wafer as a test substrate because of its smoother surface. Figures 2 and 3 shows the SEM images and AFM images of the Ag films with different thickness on the Si wafer. The morphology of Ag NPs is similar to that found on the ITO substrate, and this indicates that the surface properties of the two different substrates have little effect on the morphology of the Ag NPs. The average diameter of the Ag NPs in the 0.25 nm Ag film is about 7 nm, and the average height is about 5 nm

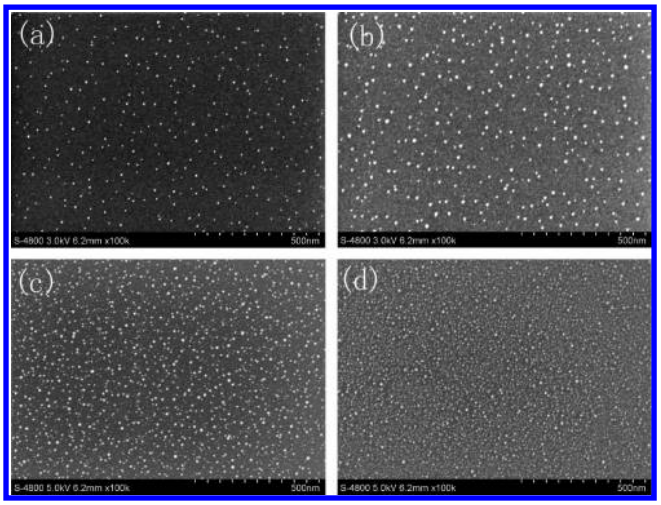

Figure 2. SEM images of (a) 0.25, (b) 0.5, (c) 1, and (d) 2 nm Ag films on a Si wafer.

(as shown in Figure 3). As the thickness of Ag film increases, both the average diameter and height of the Ag NPs increase only slightly. In contrast, the density of the Ag NPs increases gradually. The diameter of the Ag NPs in the 1 nm film ranges from 2 to 15 nm with the most probable diameter being at about 8 nm. This polydispersed NP size, which is important for the improved function of the OSCs, is observed in the thicker Ag films. This means the thermal evaporated thicker Ag films may enhance the OSCs as they can trigger LSPR over a wider wavelength range.

Figure 4 shows the absorption spectra of the Ag films with different thickness on an ITO substrate. The 0.25, 0.5, and 1 nm Ag films have a similar absorption peak at about 420 nm with an intensity increases with the film thickness. As seen in Figures 2 and 3, Ag is present as NPs, at least over the range of thicknesses investigated here. Thus any absorption should arise from the LSPR of the Ag NPs. The LSPR peak of the metal NPs is determined by their size, shape, and environment, and the LSPR peak red-shifts as the size of metal NPs increases.[16]

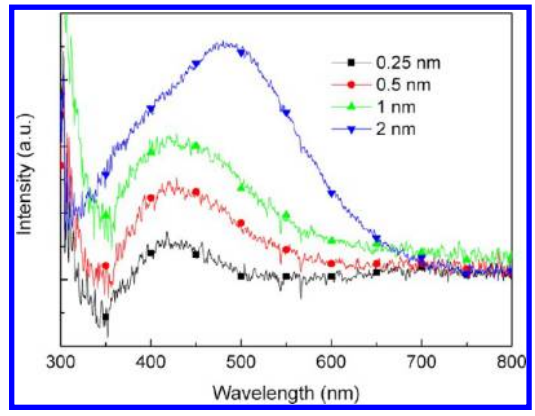

Figure 4. Absorption spectra of the Ag films with different thickness on an ITO substrate.

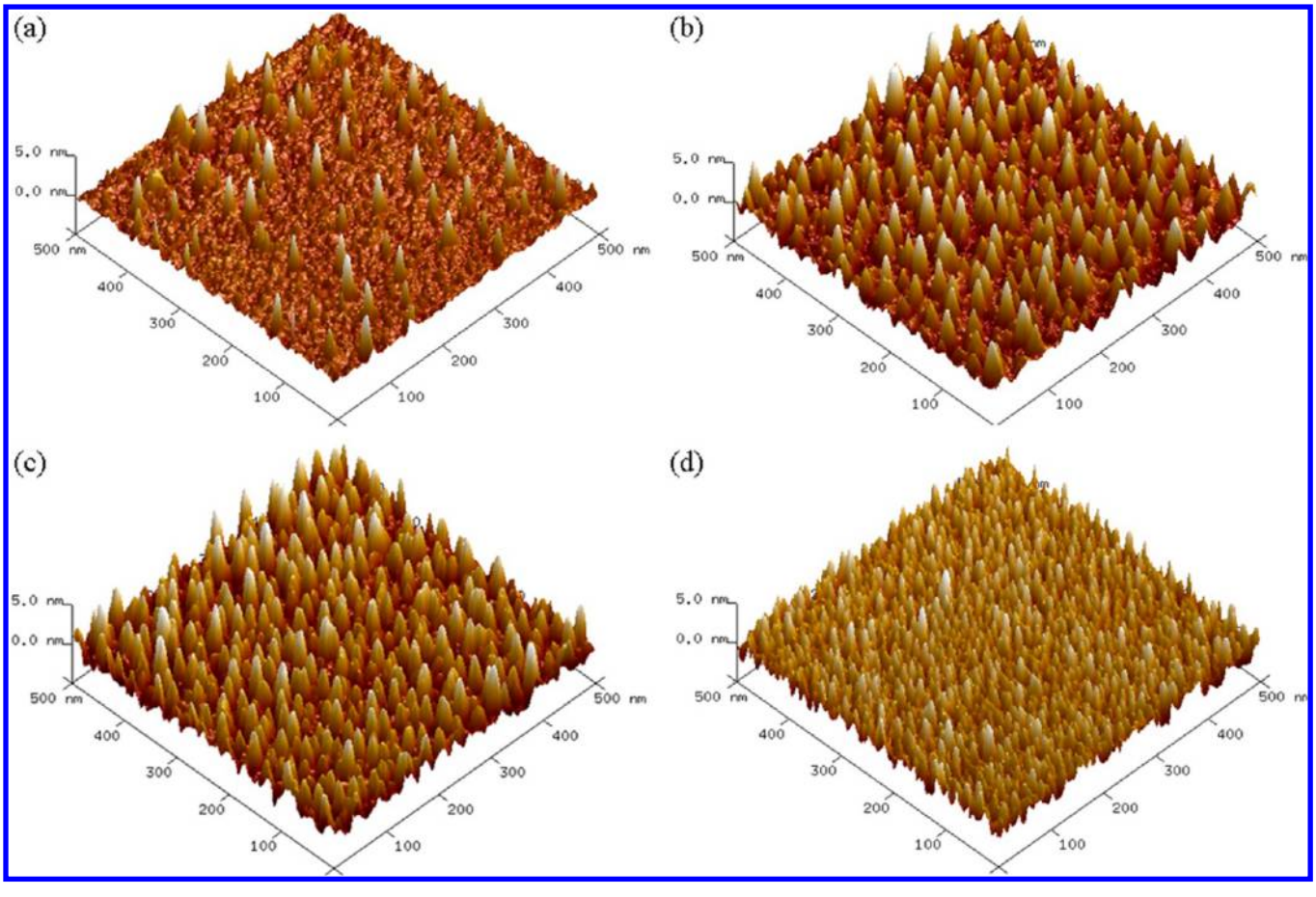

Figure 3. AFM images of (a) 0.25, (b) 0.5, (c) 1, and (d) 2 nm Ag films on a Si wafer.

These results indicate that the size of the Ag NPs changes little as the film thickness increases from 0.25 to 1 nm. However, as the thickness of Ag increases to 2 nm, the LSPR peak shifts to about 480 nm and the absorption band is broadened. The shift is attributed to the increased diameter of Ag NP and the decreased distance between the NPs, while the broadening is attributed to an enlarged Ag NP size distribution.

In the devices with a MoO_3 anode buffer layer, the device efficiencies are closely related to the thickness of the MoO_3 layer, which means it is important to confirm the relation between this thickness and the performance of the OSCs. Figures S2−S6 in the Supporting Information describe the $J-V$ curves of the OSCs with and without Ag NPs, and the data extracted from these curves are listed in Tables S1−S5 in the Supporting Information, respectively. The reference devices with different thickness of MoO_3 layer present the same V_{oc}. This indicates that the V_{oc} of the device is not affected by the thickness of MoO_3 layer. However, the V_{oc} of the devices with Ag NPs first increases with an increase in the thickness of MoO_3 layer before saturating at about 0.82 V. The V_{oc} of an OSC follows the correlation of $V_{oc} = nkt/q\ln(J_{SC}/J_0)$, where n is the ideality factor, k is the Boltzmann constant, t is the temperature, q is the fundamental charge, and J_0 is the reverse saturation current. As shown in Figures S4 and S7 in the Supporting Information, a small increase in J_{sc} and a significant decrease in J_0 are seen as the thickness of MoO_3 layer increases. In the devices with a thick MoO_3 layer, the Ag NPs can be fully covered by the MoO_3 layer. Thus the decrease in J_0 can be attributed to the prevention of charge recombination in the Ag NPs, which results in an increase of V_{oc}.[50] The optimized thickness of the MoO_3 layer of the device without Ag NPs is 2.5 nm, while they are 2.5, 5, 7.5, and 7.5 nm for the devices with 0.25, 0.5, 1, and 2 nm Ag films, respectively. It should be noted that the optimized device with 2 nm Ag shows inferior performance compared with other devices, which may be attributed to the increased probability of exciton quenching and the lower intensity of light penetrated to the organic active layer due to the increased absorption and/or back scattering by the Ag NPs with large size and high density. Figure 5 shows the

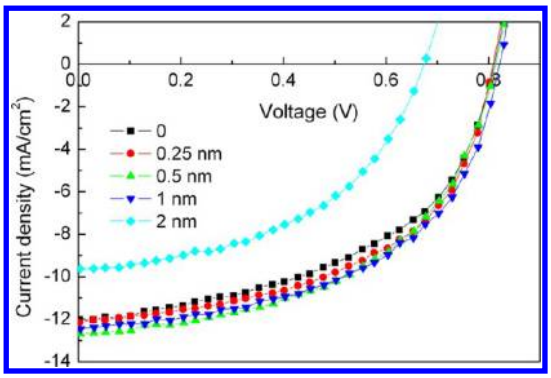

Figure 5. $J-V$ curves of the optimized devices with different thickness of Ag.

$J-V$ curves of the devices with different thickness of Ag with an optimized MoO_3 thickness. The device without Ag NPs shows a J_{sc}, V_{oc}, FF, and PCE of 0.81 V, 12.02 mA/cm^2, 0.50, and 4.89%, respectively. Such performance is comparable to a previous report.[44] With increasing Ag thickness, the PCE of the devices first increases gradually and then decreases rapidly. The optimized device with 1 nm Ag shows a J_{sc}, V_{oc}, FF, and PCE of 0.82 V, 12.45 mA/cm^2, 0.53, and 5.42%, respectively. Compared with the device without Ag NPs, the PCE is enhanced by about 11%, and such an enhancement is primary attributed to the improvement of the J_{sc} and FF of the device. On the other hand, the reference device with a 7.5 nm MoO_3 layer has a PCE of only 4.63%, as shown in Figure S2 and Tabls S1 in the Supporting Information. Thus a more pronounced enhancement in PCE of about 17% is obtained when compared with the reference device with a comparable MoO_3 layer.

Table 1. Performance of the Optimized Devices with Different Thickness of Ag

Ag thickness (nm)	J_{sc} (mA/cm^2)	V_{oc} (V)	FF	PCE (%)
0	12.02 ± 0.14	0.81 ± 0.01	0.50 ± 0.01	4.89 ± 0.16
0.25	12.16 ± 0.27	0.81 ± 0.01	0.53 ± 0.01	5.23 ± 0.06
0.5	12.67 ± 0.24	0.81 ± 0.01	0.52 ± 0.01	5.35 ± 0.18
1	12.45 ± 0.15	0.82 ± 0.01	0.53 ± 0.01	5.42 ± 0.15
2	9.62 ± 0.20	0.67 ± 0.01	0.49 ± 0.01	3.18 ± 0.17

The mechanisms of the enhanced performance of OSCs by incorporating small metal NPs usually include three aspects: first, increased hole conductivity due to the matched energy levels between the workfunction of the metal NPs and the highest occupied molecular orbital of donor materials;[22,23,28] second, increased absorption at the active layer due to the near-field enhancement of the LSPR of the metal NPs;[20,21,34−36] and third, increased probabilities of exciton dissociation due to the coupling between the excitons and the LSPR.[25] To understand these mechanisms, we carried out a further series of experiments.

Figure 6 shows the dark current of the devices, with or without 1 nm Ag, with the same MoO_3 thickness of 7.5 nm.

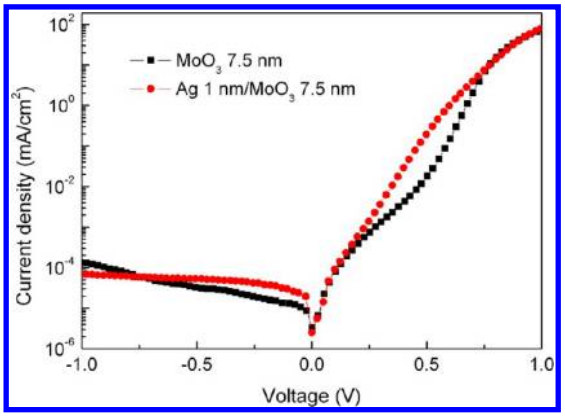

Figure 6. Comparison of the dark current of similar devices, with or without Ag NPs.

The device with Ag NPs has a higher conductivity at low voltage. Similar phenomenon has been found in other devices with different thickness of Ag. This indicates that the Ag NPs in the MoO_3 layer can act as hole transporters, which increases the conductivity of the devices.[33,35] Similar conclusions can be derived by comparison of the current of the ITO/MoO_3 (7.5 nm)/TAPC:C70 (60 nm)/TAPC (20 nm)/Ag (60 nm) hole-only devices with or without 1 nm Ag on ITO, where the device with Ag NPs shows a higher current density than the one without Ag (see Figure S8 in the Supporting Information). As a

result, the charge carrier recombination in the organic layer is reduced, which leads to an increased FF and J_{sc} in the devices.

The absorption spectra of the TAPC:C70 (60 nm) films on MoO_3 (7.5 nm) with or without 1 nm Ag are shown in Figure 7a. To eliminate the contributions of Ag NPs and/or MoO_3 absorptions on the total absorption efficiency of the films, we have excluded their absorptions by using Ag NPs/MoO_3 or MoO_3 films as the reference samples in the experiments. An increase in the absorption over the range of 400 to 800 nm is found in the devices with Ag NPs. Figure 7b shows the absorption difference (Δabs) between these two films. Enhanced absorption in the blue region with the peak located at about 445 nm and in the near-infrared region is observed in the film with Ag NPs. The Δabs peak is consistent with the LSPR of the Ag NPs in the Ag NPs/MoO_3/TAPC:C70 film, and the red-shifted LSPR peak is attributed to the change of the surrounding media by being covered with MoO_3/TAPC:C70. As the contributions that result directly from the absorptions of Ag NPs and MoO_3 have been eliminated, this enhanced absorption can be attributed to the near-field enhancement of the LSPR of the Ag NPs. The difference between the IPCE (ΔIPCE) of the devices with and without 1 nm Ag is also shown in Figure 7b. More interestingly, the curve of ΔIPCE closely follows that of Δabs. These results suggest that the enhanced absorption by the near-field enhancement of the Ag NPs is one of the factors that lead to the increased J_{sc} and hence the increased PCE of the devices.

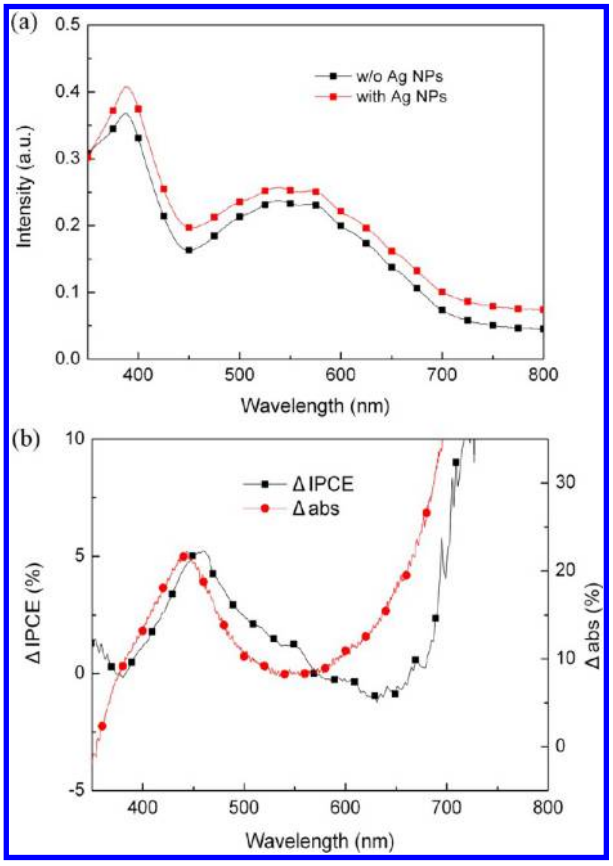

Figure 7. (a) Absorption spectra of 60 nm TAPC:C70 films on MoO_3 (7.5 nm) with and without Ag NPs. (b) Δabs of the films and ΔIPCE of the devices with and without Ag NPs.

The increased absorption can be further approved by steady state PL spectra. Figure S9 in the Supporting Information displays the absorption spectra of 40 nm TAPC, C70 and poly(3-hexylthiophene) (P3HT) films on an ITO substrate. It can be seen that almost no absorption is observed for TAPC film at the wavelength region near the LSPR peak (~430 nm) of the Ag NPs. In the devices with TAPC:C70 as the active layer, the photocurrent is primary generated by C70 because of its higher absorption efficiency in visible region and higher content in the mixture.[45] Thus TAPC:C70 or C70 films are more useful for the verification of the effects of the Ag NPs on the PL spectra. Unfortunately, the PL intensity of both these two films is beyond the detection limits of our equipment because of the low PL quantum yield of C70. Given that Ag NPs have confirmed effects on the PL spectra of TAPC:C70 or C70 films, this should also be seen when TAPC:C70 or C70 is replaced by other materials. P3HT has a high absorption efficiency in the region near the LSPR peak of the Ag NPs and a moderate PL quantum yield. Thus it was selected as a suitable replacement for C70 to investigate the effects of Ag NPs on the PL spectrum. P3HT of 20 mg/mL in 1,2-dichlorobenzene was spin-cast onto either MoO_3 (7.5 nm) or Ag (1 nm)/MoO_3 (7.5 nm) films at a speed of 4000 rad/min followed by annealed for 10 min at 120 °C. Figure 8a shows the steady-state PL spectra of the films upon excitation at 450 nm. The PL spectrum of the film without Ag NPs shows an emission peak at about 648 nm with a shoulder at about 700 nm, which can be ascribed to the P3HT emission. A 20% increase in the PL intensity was found in the film with Ag NPs, whereas the shape of the PL spectrum was unaffected. Increased PL intensity can usually be assigned

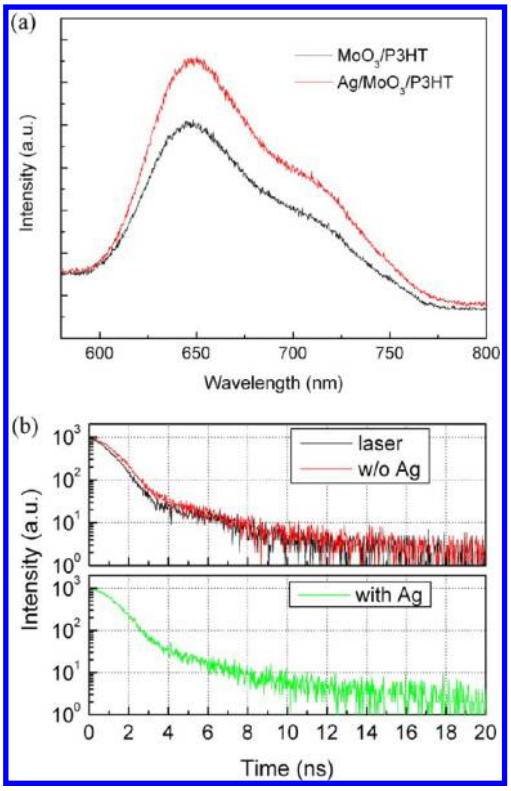

Figure 8. (a) Steady-state PL spectra of the MoO_3/P3HT films with or without Ag NPs. (b) Transient PL spectra of the MoO_3/P3HT films with or without Ag NPs; for reference, the response of the excitation laser has been provided.

to the increased absorption efficiency and/or the modified excitonic states of P3HT.[25,26] Figure 8b shows the undeconvoluted transient decay curves of the MoO_3/P3HT films with or without 1 nm Ag, and for reference, the decay of the excitation source at 648 nm is also provided. The excitation wavelength was 450 nm, which matches the LSPR of Ag NPs. The transient decays of the P3HT films with or without Ag NPs have the same profile. This means any modifications of the excitonic states of the P3HT film that are due to the coupling between the excitons and the LSPR can be neglected when a 7.5 nm MoO_3 buffer layer is used. Thus we believe that the increase in the P3HT PL intensity can be attributed to the increased light absorption and exciton generation upon excitation of the LSPR.

4. CONCLUSION

In summary, high-efficiency surface plasmon enhanced TAPC:C70 bulk heterojunction OSCs based on thermal evaporated Ag NPs have been demonstrated. In these devices, MoO_3 has been used as the anode buffer layer to avoid quenching of the excitons by Ag NPs. The optimized device with 1 nm Ag shows a PCE of 5.42%, which is 17% higher than the reference device without Ag NPs. The enhanced PCE is primary the result of improved J_{sc} and FF. The improved performance is attributed to the increased conductivity and to the increased absorption due to the near-field enhancement of the LSPR of Ag NPs. These findings indicate that such a structure may have potential as a simple and easily-processed surface plasmon enhanced OSCs, and that this structure might also be applicable to systems featuring other types of active materials.

■ ASSOCIATED CONTENT

Ⓢ Supporting Information

The SEM images of the Ag on an ITO substrate; $J-V$ curves and the data extracted from these curves of the devices with different thickness of Ag and MoO_3; dark currents of the devices with different thickness of Ag and MoO_3; and $J-V$ curves of hole-only devices. This material is available free of charge via the Internet at http://pubs.acs.org/.

■ AUTHOR INFORMATION

Corresponding Authors

*E-mail: suzs@ciomp.ac.cn.

*E-mail: chub@ciomp.ac.cn.

Notes

The authors declare no competing financial interest.

■ ACKNOWLEDGMENTS

This work was supported by the National Natural Science Foundation of China Grants 11004187, 61107082, 61076047, 61376062, and 61376022, and the Science and Technology Development Program of Jilin Province Grant 20140101094JC.

■ REFERENCES

(1) Service, R. F. *Science* **2011**, *332*, 293.
(2) Li, G.; Zhu, R.; Yang, Y. *Nat. Photonics* **2012**, *6*, 153−161.
(3) Dou, L.; You, J.; Yang, J.; Chen, C. C.; He, Y.; Murase, S.; Moriarty, T.; Enery, K.; Li, G.; Yang, Y. *Nat. Photonics* **2012**, *6*, 180−185.
(4) He, Z.; Zhong, C.; Su, S.; Xu, M.; Wu, H.; Cao, Y. *Nat. Photonics* **2012**, *6*, 591−595.
(5) You, J.; Dou, L.; Yoshimura, K.; Kato, T.; Ohya, K.; Moriarty, T.; Emery, K.; Chen, C. C.; Gao, J.; Li, G.; Yang, Y. *Nat. Commun.* **2013**, *4*, 1446.
(6) Walzer, K.; Maennig, B.; Pfeiffer, M.; Leo, L. *Chem. Rev.* **2007**, *107*, 1233−1271.
(7) Yip, H. L.; Jen, A. K. Y. *Energy Environ. Sci.* **2012**, *5*, 5994−6011.
(8) Kim, J. Y.; Kim, S. H.; Lee, H. H.; Lee, K.; Ma, W.; Gong, X.; Heeger, A. J. *Adv. Mater.* **2006**, *18*, 572−576.
(9) Lassiter, B. E.; Wei, G.; Wang, S.; Zimmerman, J. D.; Diev, V. V.; Thompson, M. E.; Forrest, S. R. *Appl. Phys. Lett.* **2011**, *98*, 243307.
(10) Na, S. I.; Kim, S. S.; Jo, J.; Oh, S. H.; Kim, J.; Kim, D. Y. *Adv. Funct. Mater.* **2008**, *18*, 3956−3963.
(11) Hu, Z.; Zhang, J.; Zhao, Y. *Appl. Phys. Lett.* **2012**, *100*, 103303.
(12) Long, Y. *Appl. Phys. Lett.* **2011**, *98*, 033301.
(13) Yu, W.; Shen, L.; Meng, F.; Long, Y.; Ruan, S.; Chen, W. *Soalr Energy Mater. Solar Cells* **2012**, *100*, 226−230.
(14) Ko, D. H.; Tumbleston, J. R.; Zhang, L.; Williams, S.; DeSimone, J. M.; Lopez, R.; Samulski, E. T. *Nano Lett.* **2009**, *9*, 2742−2746.
(15) Zhang, X. L.; Song, J. F.; Li, X. B.; Feng, J.; Sun, H. B. *Appl. Phys. Lett.* **2012**, *101*, 243901.
(16) Hutter, E.; Fendler, J. H. *Adv. Mater.* **2004**, *16*, 1685−1706.
(17) Gan, Q.; Bartoli, F. J.; Kafafi, Z. H. *Adv. Mater.* **2013**, *25*, 2385−2396.
(18) Atwater, H. A.; Polman, A. *Nat. Mater.* **2010**, *9*, 205−213.
(19) Wang, D. H.; Kim, D. Y.; Choi, K. W.; Seo, J. H.; Im, S. H.; Park, J. H.; Park, O. O.; Heeger, A. J. *Angew. Chem., Int. Ed.* **2011**, *50*, 5519−5523.
(20) Heo, M.; Cho, H.; Jung, J. W.; Jeong, J. R.; Park, S.; Kim, J. Y. *Adv. Mater.* **2011**, *23*, 5689−5693.
(21) Shahin, S.; Gangopadhyay, P.; Norwood, R. A. *Appl. Phys. Lett.* **2012**, *101*, 053109.
(22) Xie, F. X.; Choy, W. C. H.; Wang, C. C. D.; Sha, W. E. I.; Fung, D. D. S. *Appl. Phys. Lett.* **2011**, *99*, 153304.
(23) Fung, D. D. S.; Qiao, L.; Choy, W. C. H.; Wang, C.; Sha, W. E. I.; Xie, F.; He, S. *J. Mater. Chem.* **2011**, *21*, 16349−16356.
(24) Wang, D. H.; Park, K. H.; Seo, J. H.; Seifter, J.; Jion, J. H.; Kim, J. K.; Park, J. H.; Park, O. O.; Heeger, A. J. *Adv. Energy. Mater.* **2011**, *1*, 766−770.
(25) Wu, J. L.; Chen, F. C.; Hsiao, Y. S.; Chien, F. C.; Chen, P.; Kuo, C. H.; Huang, M. H.; Hsu, C. S. *ACS Nano* **2011**, *5*, 959−967.
(26) Fan, G. Q.; Zhuo, Q. Q.; Zhu, J. J.; Xu, Z. Q.; Cheng, P. P.; Li, Y. Q.; Sun, X. H.; Lee, S. T.; Tang, J. X. *J. Mater. Chem.* **2012**, *22*, 15614−15619.
(27) Kao, C. S.; Chen, F. C.; Liao, C. W.; Huang, M. H.; Hsu, C. S. *Appl. Phys. Lett.* **2012**, *101*, 193902.
(28) Chen, X.; Zuo, L.; Fu, W.; Yan, Q.; Fan, C.; Chen, H. *Solar Energy Mater. Solar Cells* **2013**, *111*, 1−8.
(29) Xu, M. F.; Zhu, X. Z.; Shi, X. B.; Liang, J.; Jin, Y.; Wang, Z. K.; Liao, L. S. *ACS Appl. Mater. Interfaces* **2013**, *5*, 2935−2942.
(30) Morfa, A. J.; Rowlen, L. L.; Reilly, T. H., III; Romero, M. J.; van de Lagemaat, J. *Appl. Phys. Lett.* **2008**, *92*, 013504.
(31) Chen, X.; Zhao, C.; Rothberg, L.; Ng, M. K. *Appl. Phys. Lett.* **2008**, *93*, 123302.
(32) Wang, X.; Ho, J. W.; Yang, Q.; Tam, H. L.; Li, G. X.; Cheah, K. W.; Zhu, F. *Org. Electron.* **2011**, *12*, 1943−1947.
(33) Kalfagiannis, N.; Karagiannidis, P. G.; Pitsalidis, C.; Panagiotopoulos, N. T.; Gravalidis, C.; Kassavetis, S.; Patsalas, P.; Logothetidis, S. *Solar Energy Mater. Solar Cells* **2012**, *104*, 165−174.
(34) Cheng, P. P.; Zhou, L.; Li, J. A.; Li, Y. Q.; Lee, S. T.; Tang, J. X. *Org. Electron.* **2013**, *14*, 2158−2163.
(35) Kim, R. S.; Zhu, J.; Park, J. H.; Li, L.; Yu, Z.; Shen, H.; Xue, M.; Wang, K. L.; Park, G.; Anderson, T. J.; Pei, Q. *Opt. Express* **2012**, *20*, 12649−12657.
(36) Spyropoulos, G. D.; Stylianakis, M. M.; Stratakis, E.; Kymakis, E. *Appl. Phys. Lett.* **2012**, *100*, 213904.
(37) Paci, B.; Generosi, A.; Albertini, V. R.; Spyropoulos, G. D.; Stratakis, E.; Kymakis, E. *Nanoscale* **2012**, *4*, 7452−7459.

(38) Salvador, M.; MacLeod, B. A.; Hess, A.; Kulkarni, A. P.; Munechika, K.; Chen, J. I. L.; Ginger, D. S. *ACS Nano* **2012**, *6*, 10024−10032.
(39) de Jong, M. P.; van IJzendoorn, L. J.; de Voigt, M. J. A. *Appl. Phys. Lett.* **2000**, *77*, 2255−2257.
(40) Meyer, J.; Shu, A.; Kröger, M.; Kahn, A. *Appl. Phys. Lett.* **2010**, *96*, 133308.
(41) Mishra, A.; Bäuerle, P. *Angew. Chem., Int. Ed.* **2012**, *51*, 2020−2067.
(42) Kyaw, A. K. K.; Wang, D. H.; Gupta, V.; Leong, W. L.; Ke, L.; Bazan, G. C.; Heeger, A. J. *ACS Nano* **2013**, *7*, 4569−4577.
(43) Zhou, J.; Zuo, Y.; Wan, X.; Long, G.; Zhang, Q.; Ni, W.; Liu, Y.; Li, Z.; He, G.; Li, C.; Kan, B.; Li, M.; Chen, Y. *J. Am. Chem. Soc.* **2013**, *135*, 8484−8487.
(44) Xiao, X.; Zimmerman, J. D.; Lassiter, B. E.; Bergemann, K. J.; Forrest, S. R. *Appl. Phys. Lett.* **2013**, *102*, 073302.
(45) Zhang, M.; Wang, H.; Tian, H.; Geng, Y.; Tang, C. W. *Adv. Mater.* **2011**, *23*, 4960−4964.
(46) Pandey, R.; Zou, Y.; Holmes, R. J. *Appl. Phys. Lett.* **2012**, *101*, 033308.
(47) Chen, G.; Sasabe, H.; Wang, Z.; Wang, X. F.; Hong, Z.; Yang, Y.; Kido, J. *Adv. Mater.* **2012**, *24*, 2768−2773.
(48) Zheng, Y. Q.; Potscavage, W. J., Jr.; Komino, T.; Hirade, M.; Adachi, J.; Adachi, C. *Appl. Phys. Lett.* **2013**, *102*, 143304.
(49) Jin, F.; Chu, B.; Li, W.; Su, Z.; Zhao, B.; Zhang, T.; Yan, X.; Gao, Y.; Wu, H.; Lee, C. S.; Zhu, J.; Pi, H.; Wang, J. *Org. Electron.* **2013**, *14*, 1130−1135.
(50) Chen, G.; Yokoyama, D.; Sasabe, H.; Hong, Z.; Yang, Y.; Kido, J. *Appl. Phys. Lett.* **2012**, *101*, 083904.